# Submicrometer All-Optical Digital Memory and Integration of Nanoscale Photonic Devices Without Isolators

Mehmet Fatih Yanik, Hatice Altug, Jelena Vuckovic, and Shanhui Fan

*Abstract*—In this paper, the authors introduce multibit all-optical memory devices in nanostructured photonic-crystal circuits using only intrinsic nonresonant optical nonlinearities of semiconductors. Introduced devices can record incoming pulses at speeds of 10 Gb/s using power levels less than 1 mW or at speeds approaching 70 Gb/s using power levels of 10 mW. The incoming pulses are recorded in high-contrast digital output levels independent of the input bit format. The devices exhibit tunable gain for fan-out with negligible reflection and low dissipation and can provide signal regeneration, including reshaping and retiming. Separate signal, clock and reset inputs, and memory outputs coexist without any crosstalk. Input, clock, and output operating frequencies can be independently tuned. By simulating the operation of such all-optical memory devices, it is also shown that nanoscale optical devices can be cascaded to construct densely integrated systems without any isolators or amplifiers, even in the presence of reflections.

*Index Terms*—Large-scale integration, optical bistability, optical isolators, optical logic devices, optical memories, photonic crystals.

## I. INTRODUCTION

**T**HE MOTIVATION for this paper is twofold. First, the development of large-scale optical networks has long been hindered by the lack of effective means for all-optical memory functions. All-optical memory is indispensable for basic functions like retiming, regeneration, reshaping, and for serial-to-parallel and parallel-to-serial conversion in time-division multiplexing. In optical communications, the header information needs to be stored for packet switching, and the entire packet needs to be stored to prevent packet dropping during congestion. Currently, optical-to-electronic (O/E) conversion is required for such storage. A fast all-optical memory can overcome the requirement of this O/E conversion and can greatly enhance both the capacity and flexibility of optical networks. Optical storage is also necessary for all-optical computing. Achieving all-optical memory function in length scales comparable to that of electronics will therefore be a major step forward in optical information processing.

Recently, Yanik *et al.* have demonstrated that both reversible and irreversible switching can be accomplished in a crossbar resonator in photonic crystals [1]. Here, using crossbar resonator switches as a building block, it is demonstrated that a digital all-optical memory capable of recording and storing multiple bits can be constructed. This memory device is extremely compact, operates at low power levels and high speeds, and performs all the logic functions that are required for an all-optical memory, including clocked recording and reset. Furthermore, its on-chip fabrication can be achieved in a single lithography mask step, and it uses only intrinsic nonlinearities in bulk semiconductors without requiring any electrical contacts or quantum wells. The introduced device can thus greatly improve the capabilities and capacities of all-optical communication networks.

Second, and from a more general perspective, it is widely believed that large-scale on-chip all-optical information processing holds the promise for the terabit communication and computing networks of the future. However, for large-scale integration of optical devices, the devices should be isolated from reflections or should at least be insensitive to reflections. Although optical isolators are considered as an option for device isolation, the requirements for the use of magnetooptical materials create serious difficulties for on-chip integration and increase circuit complexity and device dimensions dramatically.

It was recently pointed out by Soljacic *et al.* that Kerr nonlinearity can partially break the symmetry for waves propagating toward opposite directions [2]. A device with Kerr nonlinearity in general shows intensity-dependent transmission. This effect can be exploited to block a backward-propagating wave when the backward-propagating wave is sufficiently weak [2]. However, since such nonlinear devices do not provide complete optical isolation, it is unclear whether such bistable effects alone can in fact be used for large-scale device cascading.

In this paper, by implementing all-optical circuits of multibit registers, we show that all of the conditions required for large-scale device cascading and integration in the presence of reflections can be achieved using Kerr nonlinearity alone, without any isolators or power amplifiers. In this approach, the optical isolation is accomplished by combining the generic intensity-dependent responses of nonlinear devices, with a temporally irreversible behavior that is unique to the bistable optical switches in an appropriate operating regime. This approach in addition achieves amplification for fan-out and signal regeneration at each cascading stage, both of which are necessary if complex optical circuits are ever constructed.

The paper is organized as follows. First, in Section II, an in-depth discussion of the different operating modes of the crossbar resonator switches is provided, with an emphasis on those aspects that make such switches particularly useful for large-scale integration. Then, single and multibit registers are

discussed in Sections II–IV to demonstrate the operation of the proposed optical memory devices and cascading of multiple devices even in the presence of reflections.

## II. BASIC BUILDING BLOCK

The basic building block of our digital all-optical memory is the all-optical transistor recently proposed [1]. It consists of two orthogonal waveguides in a crossbar configuration and a subwavelength-scale photonic-crystal microcavity at the intersection of the two waveguides, as shown in Fig. 1. The microcavity possesses two nondegenerate and orthogonal cavity modes. Due to the symmetry of the cavity modes, each mode couples to only one of the waveguides, and the signals in the orthogonal waveguides do not have any crosstalk in either the linear or the nonlinear regime. In the presence of realistic instantaneous Kerr nonlinearity, the transmission through the microcavity exhibits bistable behavior, and signals in one of waveguides can control the transmission of the signals in the other waveguide. Using near-instantaneous Kerr nonlinearity $n_2 = 1.5 \times 10^{-17}$ W/m$^2$ in AlGaAs at wavelengths (1.55 $\mu$m) below half electronic bandgap [3], [4], such a device can operate at a few milliwatts of power levels and at speeds greater than 10 Gb/s with refractive index shifts $(\delta n/n)$ less than $10^{-3}$.

The fabrication of the crossbar structure can be achieved in a single lithography mask step using standard microfabrication techniques since it uses only intrinsic nonlinearities in semiconductors. Thus, it does not require any electrical contacts or quantum wells. A sample prototype we fabricated in Si is shown in the upper left inset of Fig. 1. The structure is fabricated on a silicon-on-insulator wafer for an operating wavelength of 1550 nm. The desired thickness of the membrane can be achieved by wafer thermal oxidization followed by hydrofluoric acid (HF) wet etching of the formed oxide layer. The fabrication process starts with spinning of the poly-methylmethacrylate (PMMA) layer with a molecular weight of 495 K on the sample surface, followed by baking on a hot plate at 170 °C for 30 min; this results in the measured PMMA thickness of 320 nm. Electron-beam lithography is then performed in a Raith-150 system at 10 keV, and the exposed PMMA is developed in a 3:1 isopropyl alcohol: methyl isobutyl ketone (IPA:MIBK) mixture for 50 s and rinsed in IPA for 30 s. Patterns are subsequently transferred to Si using magnetically induced reactive ion etch with a HBr/Cl$_2$ gas combination. After dry etching, the remaining PMMA is removed by an O$_2$ plasma process. Finally, the oxide layer underneath was removed by immersing the sample into the buffered HF, which leads to a freestanding membrane. Fabricated structures are uniform over a large area. The fabrication and experimental study of III–V semiconductor structures is in progress currently.

The optical transistor can be designed to function either as a crossbar switch (CBS), in which the presence of a control beam can reversibly switch on and off the transmission of the signal beam, or as a crossbar memory (CBM), in which the control beam generates irreversible bistable switching for the signal beam. Here, both modes of operations are used for complete memory function. Both functions are described by the same analytical model expressed in (1)–(4). This analytical model was
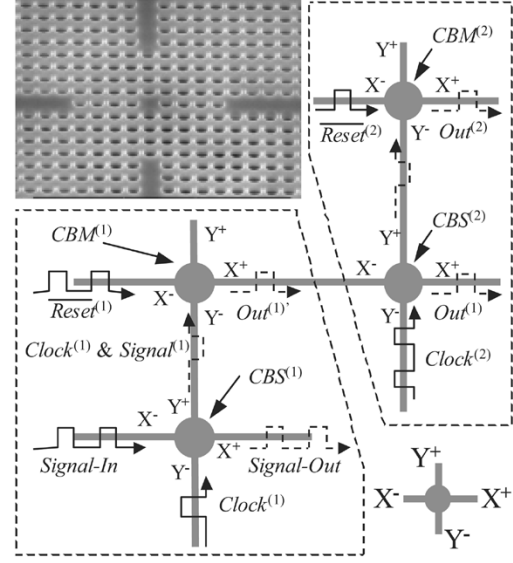


Fig. 1. Schematic of an all-optical memory device capable of registering two bits. The device consists of two cascaded single-bit registers, each encircled by a dashed line. Each single-bit register consists of optical resonators (filled gray circles) and waveguides (thick gray lines). The generic labeling of the four waveguide ports that are connected to a resonator is shown in the lower inset. The upper inset shows the scanning electron microscope (SEM) picture of a fabricated prototype crossbar microcavity in a 270-nm-thick Si membrane suspended in air. The distances between the centers of the nearest neighbor air holes are 490 nm.

verified by first-principles calculations (i.e., the finite-difference time-domain method) and is capable of simulating the entire nonlinear switching dynamics perfectly [1], [5].

$$\frac{dA_X}{dt} = i\omega_X A_X - i\gamma_X \left( \frac{|A_X|^2}{P_{XX}} + 2\frac{|A_Y|^2}{P_{XY}} \right) A_X$$
$$+ \gamma_X (S_{\text{in}X+} + S_{\text{in}X-} - A_X)$$
$$- i\gamma_X \frac{A_Y^2}{P_{XY}} A_X^* \tag{1}$$

$$\frac{dA_Y}{dt} = i\omega_Y A_Y - i\gamma_Y \left( \frac{|A_Y|^2}{P_{YY}} + 2\frac{|A_X|^2}{P_{YX}} \right) A_Y$$
$$+ \gamma_Y (S_{\text{in}Y+} + S_{\text{in}Y-} - A_Y)$$
$$- i\gamma_Y \frac{A_X^2}{P_{YX}} A_Y^* \tag{2}$$

$$S_{\text{out}X+} = -S_{\text{in}X+} + A_X \tag{3}$$

$$S_{\text{out}Y+} = -S_{\text{in}Y+} + A_Y \tag{4}$$

where $S_{\text{in(out)}X(Y)\pm}$ are proportional to the field amplitudes in the waveguides oriented along the $X(Y)$ directions such that $P_{\text{in(out)}X(Y)\pm} = |S_{\text{in(out)}X(Y)\pm}|^2$ are the input(output) powers in waveguide ports $X(Y)^{\pm}$. The subscripts $X$ and $Y$ label either the modes in waveguides that are parallel to the $x$ or the $y$ axis, respectively, or the cavity modes that couple to the corresponding waveguides. The superscripts $+(-)$ indicate the particular ports, as shown in the lower inset of Fig. 1. The field amplitudes in the cavities are proportional to $A_{X(Y)}/\sqrt{\gamma_{X(Y)}}$ such that $|A_{X(Y)}|^2$ is the total energy in the resonator modes $X$ or $Y$. By interchanging all the signs of $+$ and $-$ in (3) and (4), the equations for $S_{\text{out}X-}$ and $S_{\text{out}Y-}$ can be obtained. $P_{ij} = 1/\left[2\alpha_{ij}(\omega_i/c)^2 n_2 Q_i Q_j\right]$ are the characteristic powers

of the system, where we choose $\alpha_{XX} = 0.3$, $\alpha_{YY} = 0.3$, and $\alpha_{XY} = 0.15$, which are the self- and cross-modal overlap factors for the two cavity modes $X$ and $Y$, as described in [1] and shown in (5) at the bottom of the page, where $\mathbf{E}_{i(j)}(r) = \left[\mathbf{E}_{i(j)}(r)\exp(i\omega t) + \mathbf{E}_{i(j)}^{*}(r)\exp(-i\omega t)\right]/2$ are the electric fields in the cavity modes. $n_2$, $\omega_{X(Y)}$, $a$, and $c$ are the instantaneous Kerr nonlinearity coefficient, the angular frequencies of the cavity modes $X(Y)$, the lattice constant of the photonic crystal, and the speed of the light, respectively. $\gamma_{X(Y)} = \omega_{X(Y)}/2Q_{X(Y)}$ are the total in-plane coupling rates of cavity modes to the corresponding waveguide. $\delta_{X(Y)} \equiv (\omega_{X(Y)} - \omega_{inX(Y)})/\gamma_{X(Y)}$ are the detunings of the cavity resonances from the carrier frequencies of the signals in the waveguides. The last terms on the right-hand side of (1) and (2) describe a nonlinear energy exchange process between the control and the signal, which become negligible when the frequencies of the signal and control inputs and the corresponding resonances of the cavity modes are separated by more than the width of the resonances.

The quality factors and the detunings of the microcavities determine threshold power levels, the switching speeds of the system, and the maximum output contrasts [1]. In particular, the detunings $\delta_{X,Y}$ set the relative shape of the bistability curves. If the input is only in either the $X$ or $Y$ waveguide, bistable behavior occurs when $\delta_{X(Y)} \geq \sqrt{3}$. At a given normalized detuning, the switching power levels are inversely proportional to $Q_{X,Y}^2$, and the speed of the switching scales linearly with $Q_{X,Y}$ [1]. By controlling the feedback dynamics, they also determine which of the waveguide inputs ($X$ or $Y$) control the transmission of the other waveguide and whether the device exhibits memory behavior or not [1]. Thus, simply choosing the appropriate structural parameters enables different devices (i.e., CBS and CBM) with the same crossbar device architecture.

We first describe the operation of individual CBS and CBM elements shown in Fig. 1. CBS accepts two inputs from $X^-$ and $Y^-$ ports and produces an AND operation on the inputs at the $Y^+$ output port. Fig. 2(a) shows the $Y^-$ input versus $Y^+$ output of CBS in the presence and the absence of the $X^-$ input in steady state. The detuning for the $Y$ ports $\delta_Y = 1.0$ and the in-plane quality factor $Q_Y = 2000$ are chosen such that no bistable memory effect is present in the bistability curve of Fig. 2(a). Nevertheless, the transmitted power through $Y$ ports can still be modulated with sufficient contrast by the $X^-$ input. The $Y^+$ output reversibly switches to higher or lower power in the presence or absence of the $X^-$ input due to nonlinear modulation of the refractive index; thus, it acts as an AND gate without any bistability. Fig. 2(b) shows the $X^-$ input versus $X^+$ output of CBS in the presence and the absence of the $Y^-$ input in steady state. With the choice of a relatively low in-plane quality factor $Q_X = 500$ for the $X$ ports, and a small detuning

$\delta_X = 0.2$, no significant reflection occurs through $X$ port due to nonlinear frequency shifts, and the transmission is close to unity for a wide range of $X^-$, and $Y^-$ input powers.

The CBM functions as a memory device: at an appropriate supply power level from the $X^-$ port, the $X^+$ output becomes high at the rising edge of $Y^-$ input and stays at a high level even after the $Y^-$ input returns to zero. The $X^+$ output returns to its initial state (i.e., $X^+ = 0$) only when the supply power from $X^-$ port is turned off. Such operation is achieved with the choice of a large detuning $\delta_X = 2.0$ and a relatively high in-plane quality factor of $Q_X = 2000$. The details of the device operation are shown in Fig. 2(c). The $X^+$ output exhibits a high-contrast bistable dependency to the $X^-$ input. The shape of such bistable transmission curves can be controlled by the $Y^-$ input. By choosing an $X^-$ input power within the bistable regime [Fig. 2(c)] when the $Y^-$ input is zero, the $X^+$ output power can be switched from low to high (but not the other way around) when the $Y^-$ input is applied. Suppose that the $X^+$ output power is initially in a low power level, when the rising edge of the $Y^-$ input exceeds a certain threshold power, the bistable transmission curve of the $Y$ port is sufficiently shifted to the left, as shown in Fig. 2(c), resulting in a bistable (digital) switching to higher output power. After such switching occurs, only the high transmission state is allowed. Even after the $Y^-$ input turns off, the $X^+$ output stays high; thus, this process is irreversible, and the CBM records whether the inputs from the two ports concurrently crossed a certain power threshold, thus exhibiting memory effects. Such irreversibility provides signal isolation: a small reflection of the $X^+$ output back into the $X^+$ input cannot switch the CBM back to a lower transmission state. Although such signal isolation is incomplete (when the reflected signal is large, the switching of CBM to the lower state may indeed occur and disrupt the memory function), it is in fact sufficient to allow for large-scale cascading, as we will see later. The memory of the CBM can be erased by briefly turning off the input power to the $X^-$ port and then turning on the $X^-$ input power back to its normal level. This returns the output at the $X^+$ port to the lower level. The CBM device exhibits signal gain: a small variation in the signal power at the $Y^-$ input can result in a large variation at the $X^+$ output [Fig. 2(c)], which is important for fan-out applications. This is accomplished with the choice of a small $\delta_Y = 0.7$ and a relatively in-plane quality factor $Q_Y = 2000$ for $Y$ ports. The choice of $\delta_Y$ counterbalances the negative feedback process occurring during the switching process that would otherwise cause significant rejection of the $Y^-$ input power out of the cavity before irreversible switching of CBM occurs. The choice of large $Q_Y$ enables significant energy buildup in the $Y$ cavity mode of CBM and allows significant shift of the bistable transmission curve of the $X$ port [Fig. 2(c)] with rather low $Y^-$ input power. Furthermore, it is

$$\alpha_{ij} = \left(\frac{c}{\omega_i}\right)^d \frac{\int_{\text{vol}} d^d r\left[|\mathbf{E}_i(r)\cdot\mathbf{E}_j(r)|^2 + 2|\mathbf{E}_i(r)\cdot\mathbf{E}_j^*(r)|^2\right]n^2(r)n_2(r)}{\left[\int_{\text{vol}} d^d r|\mathbf{E}_i(r)|^2 n^2(r)\right]\left[\int_{\text{vol}} d^d r|\mathbf{E}_j(r)|^2 n^2(r)\right]n_2(r)_{\max}} \tag{5}$$
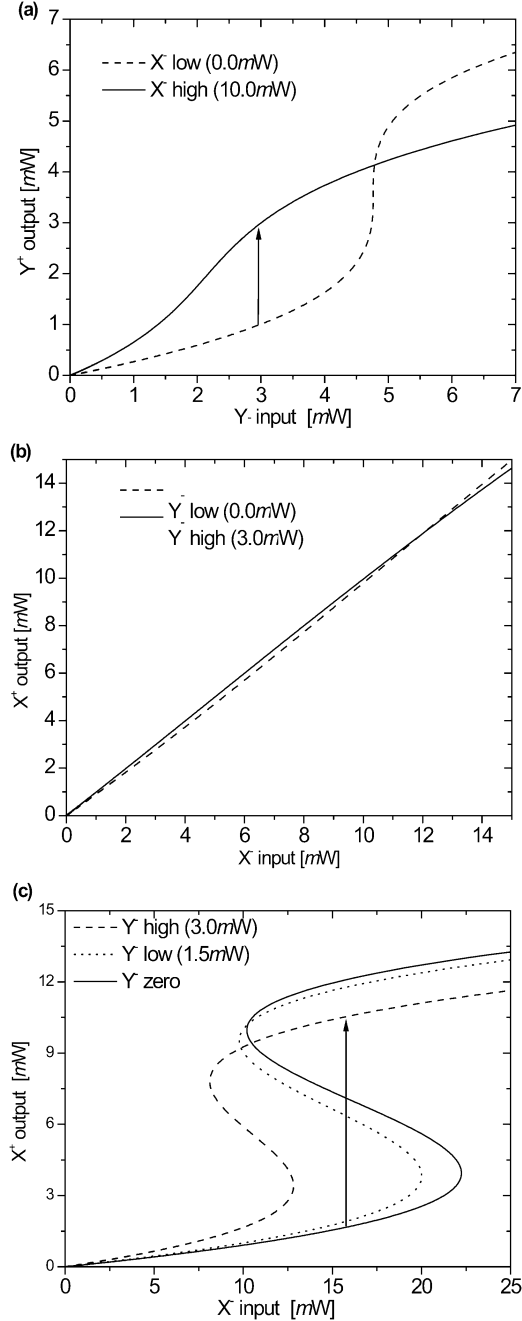
Fig. 2. (a) and (b) exhibits the operation of a CBS, and (c) exhibits the operation of a CBM. (a) $Y^-$ input versus $Y^+$ output of CBS, in the presence or absence of $X^-$ input. The $Y^+$ output reversibly switches between a higher and a lower level in the presence or absence of the $X^-$ input; thus, it acts like a low-contrast AND gate without any memory. (b) $X^-$ input versus $X^+$ output of CBS, in the presence or absence of $Y^-$ input. The transmission through $X$ ports is close to unity for a large range of $Y^-$ input powers, indicating small reflection. (c) $X^-$ input versus $X^+$ output of CBM in the presence of varying powers of $Y^-$ input. The switching to a higher output power level occurs if and only if the $Y^-$ input of CBM exceeds a certain threshold power. Once the output is at high power, it cannot return to low transmission, even when the $Y^-$ input turns off. The output power can be reset to zero only by turning off the $X^-$ input.

possible to obtain an arbitrarily large output gain for fan-out simply by increasing both supply power through the $X^-$ port and the detuning of CBM.

## III. SINGLE-BIT REGISTER

An ideal memory element should be able to record incoming bits when triggered by a clock signal and should be erasable. For noise immunity, the device should be digital where the output switches among several discrete power levels only when the input and clock powers exceed certain power thresholds. Furthermore, there should not be any crosstalk between the signal, clock, and erase inputs and outputs. We construct such a memory in Fig. 1 using the CBS and the CBM elements. The $Y^+$ output port of a CBS is connected to the $Y^-$ input port of a CBM element via a single-mode photonic-crystal waveguide. The signal input is sent through the $X^-$ input port of the CBS, and the clock input is sent through the $Y^-$ input port of CBS. The $X^-$ input port of the CBM connects to the supply/reset input. The $Y^+$ output of the CBS switches to a high power level only when both signal and clock inputs are high. Such a high-power output from the CBS in turn switches the CBM to a high transmission state irreversibly. This process results in a clocked recording of a single input bit in the $X^+$ output state of the CBM.

The bistable switching in the CBM causes strong feedback in the $Y^-$ port of the CBM. Consequently, nonnegligible reflection occurs between the CBS and the CBM. Such reflection needs to be taken into account accurately in order to model the correct switching dynamics of the structure. We model the operation of the cascaded device by coupling the outputs and inputs of the crossbar devices using scattering theory and solving the coupled nonlinear dynamics self-consistently. Propagation along the single-mode waveguide is taken into account as a phase lag $\phi$, which can be designed by choosing the appropriate waveguide lengths. The coupling between the two crossbar devices $a$ and $b$ through the single-mode waveguide can be expressed simply using the scattering matrixes

$$S^a_{\text{in},i+} = S^b_{\text{out},j-}e^{-i\phi} \qquad (6)$$

$$S^b_{\text{in},j-} = S^a_{\text{out},i+}e^{-i\phi} \qquad (7)$$

where the coupling occurs between the output port $i^+$ of crossbar $a$ and the input port $j^-$ of crossbar $b$. In general, $\phi$ is frequency dependent. However, since the signal bandwidth is narrow with respect to carrier frequencies, the frequency dependency of $\phi$ across the signal bandwidth can be ignored. Our numerical simulations indicate that $\phi = 0.8\pi + 2\pi N$ produces the optimal switching behavior. We note that this is not a Fabry–Pérot resonance condition with respect to the length of the connecting waveguide, and significant amplitude buildup in the connecting waveguide does not occur, which would otherwise lead to nonlinear effects in the waveguide. The simulations also indicate that the switching behavior is in fact not sensitive to the variation of $\phi$; indeed, a 20% variation in $\phi$ still produces the correct switching behavior. Equations (3)–(7) are used to eliminate in (1) and (2) the input and output amplitudes (e.g., $S^a_{\text{in},i+}$) in the waveguides that connect the two devices, to obtain a pair of coupled nonlinear differential equations in terms of the resonant mode amplitudes $A$'s. Then, stiff differential equation solvers are used to step through time and simulate the dynamic behavior of the coupled device.
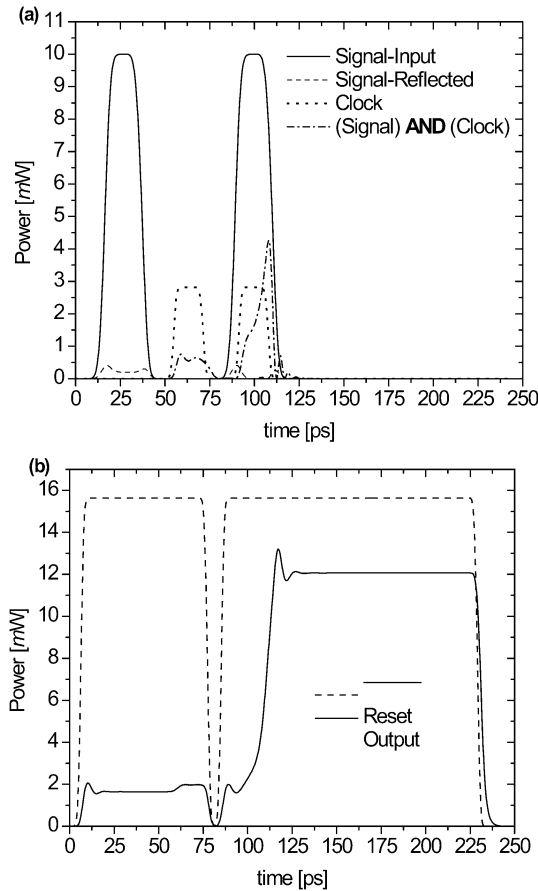
Fig. 3. Single-bit register records the last bit (1) of a 3-b pulse sequence (101). (a) Signal input ($P_{\text{Signal-In}}$), clock ($P_{\text{Clock}}$), reflected signal ($P_{\text{Signal-Ref}}$), and transmitted clock power ($P_{\text{Signal}\wedge\text{Clock}}$) as a function of time. (b) Reset ($P_{\overline{\text{Reset}}}$) and output ($P_{\text{Output}}$) powers as a function of time. The output switches to high power when both signal and clock is high and is reset by turning off $P_{\overline{\text{Reset}}}$.

The simulation results using (1)–(7) on a single-bit memory element consisting of cascading CBS and CBM are shown in Fig. 3. (We refer to such a single-bit memory as CBS-M.) Two signal pulses, centered at $t = 25$ and $100$ ps, respectively, are sent in through the $X^-$ port of the CBS element, as represented by "Signal-In" in Fig. 1. In addition, two clock pulses are sent in through the $Y^-$ port of the CBS element, centered at $t = 62.5$ and $100$ ps, as represented by $P_{\text{Clock}}$ in Fig. 1. The timings of signal and clock pulses are chosen to illustrate different dynamic regimes of the device. Between $t = 0$ and $50$ ps, only the signal pulse is present; therefore, the clock input is low, and the $P_{\text{Signal}\wedge\text{Clock}}$ output is also low [Fig. 3(a)] since there is no crosstalk between the $P_{\text{Signal}\wedge\text{Clock}}$ output and $P_{\text{Signal-In}}$ input. The output of the CBM is at a low level [Fig. 3(b)]. Between $t = 50$ and $80$ ps, the clock pulse is present while the signal pulse is absent. The high clock input (i.e., $t = 60$ ps) causes the $P_{\text{Signal}\wedge\text{Clock}}$ output to increase slightly, but this increase alone is not sufficient to switch the CBM, except a small transient increase in the output $P_{\text{Output}}$ at $t = 65$ ps. The output of the CBM again remains at the low level after the clock pulse has passed through such that a low signal input is recorded as a low output power in CBM. The memory is reset by turning off the reset input $P_{\overline{\text{Reset}}}$ at $t = 80$ ps before the next clock signal is applied. Between $t = 80$ and $120$ ps, both the clock and the

signal inputs are high, and the output $P_{\text{Signal}\wedge\text{Clock}}$ rises above the switching power threshold of the CBM, causing the output of the CBM to switch to high power at $t = 100$ ps. (Note that the $P_{\text{Signal}\wedge\text{Clock}}$ output can exceed $P_{\text{Clock}}$ input because of the reflections between the CBS and the CBM.) The output of the CBM remains at a high level after both the clock and the signal pulse has passed through. Thus, the bit in the signal is recorded in the output of the CBM. We note that the clock and the signal inputs do not need to be perfectly synchronized—as long as the clock and the signal inputs overlap partially in time, the CBM can switch to the higher transmission state. Finally, the device can be reset by turning off the reset input, as we have done at $t = 230$ ps, which returns the output of the device to the low power level. Thus, our device accomplishes all the functions required for a single-bit register.

## IV. Large-Scale Integration and Multibit Register

For large-scale integration, memory and logic devices should be cascadable, which introduces important constraints on the devices used. In particular, if large numbers of elements need to be cascaded, the devices must provide output gain for fan-out and must digitally regenerate the signals. In addition, since reflections are almost inevitable, and the use of isolators requires materials that are difficult to integrate on-chip, it is essential that the devices should work in the presence of the reflections. In the optical memory proposed here, since the signal input to the CBS exhibits almost no reflection, and since the CBM output has gain with irreversible digital transitions, the single-bit memory elements can be cascaded to provide multibit optical memory functions on-chip without any optical isolation or additional amplification.

To demonstrate the cascadability of the introduced devices, we first construct a 2- register by coupling the output of a first single-bit register ($\text{CBS}^{(1)}$-$\text{M}^{(1)}$) to the input of a second register ($\text{CBS}^{(2)}$-$\text{M}^{(2)}$), as shown in Fig. 1. The 2-b register is simulated in a similar fashion as in the single-bit register by expressing the amplitudes inside all internal connecting waveguide sections in terms of the amplitudes in the resonators and by solving the resulting ordinary differential equations that describes the amplitudes of the resonators. To demonstrate the operation of the cascaded device, we input a 5-b pulse sequence of (11010) during the time intervals shown in Fig. 4(a) and clock the first register at the second and third intervals to record two bits (10) from the data stream [Fig. 4(b)]. At the first rising edge of the clock inputs $P_{\text{Clock}}^{(1)}$ ($t = 70$ ps) [Fig. 4(b)], the register $\text{CBS}^{(1)}$-$\text{M}^{(1)}$ captures the first input signal bit (1) and fetches it to the output $P_{\text{Output}}^{(1)}$ of $\text{CBM}^{(1)}$ (between $t$=70 ps and $t = 85$ ps in Fig. 4(b)). $P_{\text{Output}}^{(1)}$ is subsequently read by the next register ($\text{CBS}^{(2)}$-$\text{M}^{(2)}$) by the second clock $P_{\text{Clock}}^{(2)}$ after $t$=75 ps [Fig. 4(c)], which switches the output $P_{\text{Output}}^{(2)}$ to a high level ($t > 100$ ps) and thus records the clocked bit. After its output is read by the second register, the $\text{CBM}^{(1)}$ is then reset by briefly turning off and then turning on $P_{\overline{\text{Reset}}}^{(1)}$ back to the previous high level at $t = 90$ ps [Fig. 4(b)]. This negative pulse erases the memory of $\text{CBM}^{(1)}$ by returning the output
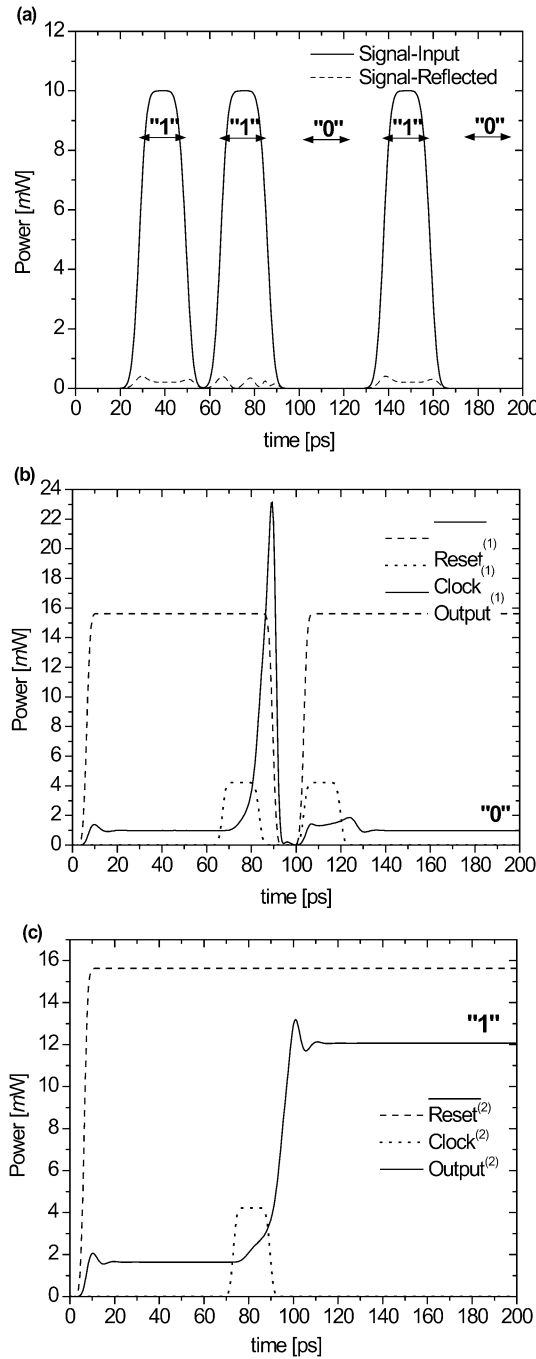
Fig. 4. Two-bit register records from a 5-b-long pulse sequence (11010) the second and the third bits (10). (a) Signal input $\left(P_{\text{Signal-In}}^{(1)}\right)$ and reflection $\left(P_{\text{Signal-Ref}}^{(1)}\right)$ at the first register as a function of time. (b) Clock $\left(P_{\text{Clock}}^{(1)}\right)$ and reset $\left(P_{\text{Reset}}^{(1)}\right)$ inputs and output $\left(P_{\text{Output}}^{(1)}\right)$ of the first register as a function of time. (c) Clock $\left(P_{\text{Clock}}^{(2)}\right)$ and reset $\left(P_{\text{Reset}}^{(2)}\right)$ inputs and memory output $\left(P_{\text{Output}}^{(2)}\right)$ of the second register as a function time. At the end of the two clock cycles, the bits (10) are recorded in the output power levels ($P_{\text{Output}}^{(1)}$ and $P_{\text{Output}}^{(2)}$) of CBM$^{(1)}$ and CBM$^{(2)}$.

of CBM$^{(1)}$ to a low level. After the reset pulse has passed, CBM$^{(1)}$ is ready to read the next incoming bit (0) during the clocked interval between $t = 100$ and 120 ps. During the second clocked interval of the first register ($t = 105$ ps to $t = 120$ ps), the next signal bit (0) is registered to the

output $P_{\text{Output}}^{(1)}$ of CBM$^{(1)}$, which leaves $P_{\text{Output}}^{(1)}$ at low power ($t > 130$ ps). No recording operation occurs except in the clocked intervals, demonstrating the clocked operation of the cascaded device.

This sequential mechanism of registering and shifting the serial input bit streams to multiple registers is readily applicable to arbitrary numbers of registers. In addition, we have indeed simulated multibit registers, which exhibit similar switching behaviors. Since the CBS-M switches only when both the clock and the input signals are high, the outputs are synchronized with the clock signals. Furthermore, since the outputs switch only between two distinct power levels when the input pulses cross certain power thresholds, the distorted input pulses are reshaped and amplified. These synchronization (retiming), reshaping, and amplification processes enable regeneration of signals at each stage.

The record speed is limited by the 15-ps rise and delay times between the register outputs for the quality factors used here; thus, these devices can fetch input pulses at speeds approaching 70 Gb/s using 10 mW of signal power and a few milliwatts of clock power. In this device, within the constraint of a maximal index shift allowed by the materials, the switching speed and the power requirement is inversely related. This can be seen as follows: the ratios of the energies in the cavity modes to the powers in the waveguides are linearly proportional to the coupling quality factor [1], [6]. Since the index shifts required to change transmission are also inversely proportional to the coupling quality factors [1], [6], the power levels scale inversely with the square of the quality factors. By simply scaling all the quality factors with the same ratio, the same switching behavior is retained for the same detuning. The switching times depend linearly on the coupling quality factors. Therefore, for the same detunings, the required power levels and the maximum switching speeds are quadratically related. Thus, one can thus accomplish design tradeoff between power levels and switching speeds [1]. For example, the signal power requirement in our proposed device can be reduced to less than 1 mW at 10 Gb/s by decreasing the coupling of the microcavities to the waveguides in the entire circuit.

Within the crossbar microcavity, the electric field is dramatically enhanced, and our FDTD simulations indicate that for the maximum 10-mW average power at 70 Gb/s, the instantaneous peak electric field value in the cavity reaches $3 \cdot 10^7$ V/m [1], [5]. In addition, the peak intensity level in the cavity is about 0.1 GW/cm$^2$, which is in fact an order of magnitude lower than the power level used in typical nonlinear guided wave experiments [7]. Since the carrier frequencies are below the middle of the electronic bandgap and since the semiconductors are undoped, the losses due to linear absorption and multiphoton processes are sufficiently suppressed. Because of the large surface-to-volume ratio of these microcavities, we also do not expect the thermal heating due to any weak loss mechanism to be a significant problem.

The *difference* between the resonance frequencies of the microcavities should not deviate more than a small fraction of the coupling rates of the cavities to the waveguides, which is on the order of $\delta f = 100$ GHz. For a small fabrication error yielding a removal or addition of a dielectric material with area $A_{\text{def}}$

and dielectric constant $\delta\varepsilon$, perturbation theory [8] predicts that a cavity resonance frequency $f$ should shift by an amount $\delta f$ given by

$$\frac{\delta f}{f} \approx \frac{\delta\varepsilon A_{\text{def}}}{2\varepsilon_{\text{av}} A_{\text{mod}}} \qquad (8)$$

where $\varepsilon_{\text{av}}$ is the average dielectric constant over the cavity modal area $A_{\text{mod}}$. Here, for simplicity, we assumed that $|\nabla \times H|^2$ is uniform over the cavity modal area. Note that our assumption actually overestimates $\delta f$ since the perturbation in a cavity structure as shown in the inset of Fig. 1 would occur in the holes near the cavity boundary where the cavity field is smaller. In electron-beam or ion-beam lithography, *relative* structural deviations among cavities due to beam deviations are on the order of a few nanometers and would not shift resonance frequencies noticeably. The biggest source of relative structural deviations arise from surface roughness due to beam scattering in the resist and etching, and although these deviations are on the order of 1–10 nm, the correlation lengths of such errors are less than 20 nm, and within the entire cavity modal area, we expect such deviations to average to zero except small fluctuations with a total defect area on the order of $A_{\text{def}} \approx \times\, 10$ nm. For $A_{\text{mod}} \approx 1\ \mu m^2$, $\varepsilon_{\text{av}} \approx 10$, $\delta\varepsilon \approx 10$, such a defect would lead to a frequency deviation of $\delta f \approx 4$ GHz in a cavity resonance centered at $f = 200$ THz. Since such frequency deviations are much less than the cavity coupling rates to the waveguides, our devices can still perform their function. Furthermore, the fabrication requirements can be relaxed if the cavity resonance frequencies can be slightly tuned after fabrication. In photonic-crystal slab structures, tunable frequency shifts as large as 1 THz have in fact been demonstrated [9].

Although for simplicity we have not included cavity losses in our calculations, the effects of such losses can be modeled in a standard fashion by adding an additional amplitude decay rate in the coupled mode (1) and (2) [6]. Our simulations showed that as long as the losses are a factor of three or more lower than coupling rates between the cavities and the waveguides, the bistable behaviors we presented here are still clearly observable, and the bistable memory devices can still work. Considering that cavity quality factors for dipole modes greater than $2 \cdot 10^4$ are achievable in photonic-crystal microcavities [10], we expect our devices to function as predicted.

## V. CONCLUSION

In summary, optical memory devices in photonic crystals that are ideally suitable for large-scale on-chip integration were introduced in this paper. The signal input experiences negligible reflection, and the digital output levels show no deterioration at all after being processed through multiple stages of registers. The signals are regenerated (i.e., reshaped and retimed) at each stage. The power gains can be simply tuned for larger fan-out. In addition, slight errors in the cavity resonance frequencies or power levels do not deteriorate the performance of the registers, since the switching occurs digitally by threshold-dependent irreversible bistable transitions. By showing cascaded optical registers using subwavelength scale resonators, the fundamental fea-

sibility of large-scale integration of nanoscale photonic devices without optical isolators has also been demonstrated,

## REFERENCES

[1] M. F. Yanik, S. Fan, M. Soljacic, and J. D. Joannopoulos, "All-optical transistor action with bistable switching in a photonic crystal cross-waveguide geometry," *Opt. Lett.*, vol. 28, pp. 2506–2506, 2003.

[2] M. Soljacic, C. Luo, J. D. Joannopoulos, and S. Fan, "Nonlinear photonic crystal microdevices for optical integration," *Opt. Lett.*, vol. 28, pp. 637–637, 2003.

[3] M. N. Islam, C. E. Soccolich, R. E. Slusher, A. F. J. Levi, W. S. Hobson, and M. G. Young, "Nonlinear spectroscopy near half-gap in bulk and quantum well GaAs/AlGaAs waveguides," *J. Appl. Phys.*, vol. 71, pp. 1927–1927, 1992.

[4] A. Villeneuve, C. C. Yang, G. I. Stegeman, C. Lin, and H. Lin, "Nonlinear refractive-index and two photon-absorption near half the band gap in AlGaAs," *Appl. Phys.*, vol. 62, pp. 2465–2465, 1993.

[5] M. F. Yanik, S. Fan, and M. Soljacic, "High contrast all-optical bistable switching in photonic crystals microcavities," *Appl. Phys. Lett.*, vol. 83, pp. 2739–2739, 2003.

[6] H. A. Haus, *Waves and Fields in Optoelectronics*.   Englewood Cliffs, NJ: Prentice-Hall, 1984.

[7] G. I. Stegeman, "Nonlinear guided wave optics," in *Contemporary Nonlinear Optics*, G. P. Agrawal and R. W. Boyd, Eds.   San Diego, CA: Academic, 1992, pp. 1–40.

[8] S. G. Johnson, M. Ibanescu, M. A. Skorobogatiy, O. Weisberg, J. D. Joannopoulos, and Y. Fink, "Perturbation theory for Maxwell's equations with shifting material boundaries," *Phys. Rev. E, Stat. Phys. Plasmas Fluids Relat. Interdiscip. Top.*, vol. 65, pp. 066 611–066 611, 2002.

[9] F. Raineri *et al.*, "Nonlinear 2D semiconductor photonic crystals," presented at the Conf. Lasers Electro-Optics, San Francisco, CA, May 20, 2004.

[10] M. Loncar, M. Hochberg, A. Scherer, and Y. Qiu, "High quality factors and room-temperature lasing in a modified single-defect photonic crystal cavity," *Opt. Lett.*, vol. 29, pp. 721–721, 2004.

**Mehmet Fatih Yanik** received the B.S. degree in electrical engineering and physics and the Master's degree from the Massachusetts Institute of Technology (MIT), Cambridge, in 1999 and 2000, respectively, with a thesis on ultrafast electron spin dynamics. He is currently working toward the Ph.D. degree in applied physics at Stanford University, Stanford, CA.

He has worked on quantum computing at Xerox Parc and on molecular electronics at HP Laboratories. He is currently working on nanophotonics and femtosecond laser nanosurgery.

**Hatice Altug** received the B.S. degree in physics from Bilkent University, Ankara, Turkey, in 2000. She is currently working toward the Ph.D. degree in applied physics at Stanford University, Stanford, CA.

Her current research interest includes the design and fabrication of photonic-crystal devices.

**Jelena Vuckovic** received the Ph.D. degree in electrical engineering from the California Institute of Technology, Pasadena, in 2002.

She is currently an Assistant Professor in electrical engineering at Stanford University, Stanford, CA, since 2003. Her research interests include nanoscale and quantum photonics.

**Shanhui Fan** received the Ph.D. degree in theoretical condensed matter physics from the Massachusetts Institute of Technology (MIT), Cambridge, in 1997.

He was a Research Scientist at the MIT Research Laboratory of Electronics. He has been an Assistant Professor in electrical engineering at Stanford University, Stanford, CA, since 2001. His research interests include computational studies of nanophotonic systems.